LETTER

https://doi.org/10.1038/s41586-018-0503-6

Absolute timing of the photoelectric effect

M. Ossiander[1,2,5]*, J. Riemensberger[1,2,5], S. Neppl[3], M. Mittermair[1], M. Schäffer[1,2], A. Duensing[1], M. S. Wagner[1], R. Heider[1], M. Wurzer[1], M. Gerl[1,2], M. Schnitzenbaumer[1], J. V. Barth[1], F. Libisch[4], C. Lemell[4], J. Burgdörfer[4], P. Feulner[1] & R. Kienberger[1,2]*

Photoemission spectroscopy is central to understanding the inner workings of condensed matter, from simple metals and semiconductors to complex materials such as Mott insulators and superconductors[1]. Most state-of-the-art knowledge about such solids stems from spectroscopic investigations, and use of subfemtosecond light pulses can provide a time-domain perspective. For example, attosecond (10^{-18} seconds) metrology allows electron wave packet creation, transport and scattering to be followed on atomic length scales and on attosecond timescales[2–7]. However, previous studies could not disclose the duration of these processes, because the arrival time of the photons was not known with attosecond precision. Here we show that this main source of ambiguity can be overcome by introducing the atomic chronoscope method, which references all measured timings to the moment of light-pulse arrival and therefore provides absolute timing of the processes under scrutiny. Our proof-of-principle experiment reveals that photoemission from the tungsten conduction band can proceed faster than previously anticipated. By contrast, the duration of electron emanation from core states is correctly described by semiclassical modelling. These findings highlight the necessity of treating the origin, initial excitation and transport of electrons in advanced modelling of the attosecond response of solids, and our absolute data provide a benchmark. Starting from a robustly characterized surface, we then extend attosecond spectroscopy towards isolating the emission properties of atomic adsorbates on surfaces and demonstrate that these act as photoemitters with instantaneous response. We also find that the tungsten core-electron timing remains unchanged by the adsorption of less than one monolayer of dielectric atoms, providing a starting point for the exploration of excitation and charge migration in technologically and biologically relevant adsorbate systems.

Two complementary methods of attosecond metrology, namely, the attosecond streak camera[8] and RABITT interferometry[9], are capable of providing attosecond-scale timing information on electron emission. The ultimate aim—to determine the absolute duration of the photoelectric effect from a solid, that is, the temporal sequence of events between the arrival time of an ionizing extreme-ultraviolet (XUV) photon at its surface and photoelectron emission into vacuum—has remained a major challenge. Here we report an approach that can overcome this difficulty: by using adsorbed atoms as a chronoscope whose absolute photoionization timing can be determined in concurrent gas-phase measurements, the absolute timing of photoemission from solid surfaces can now be clocked with attosecond precision. As proof of the concept, we examine the photoelectric effect for the dense-packed W(110) surface of a tungsten crystal at 105 eV photon energy using an attosecond streak camera. The measurement geometry is depicted in Fig. 1a. We adsorb iodine atoms on a metallic surface: these atoms serve as chronoscope species. When the XUV light pulse arrives at the surface, it stimulates electron expulsion from these clock atoms. The appearance of these electrons in the ionization continuum marks the light pulse's arrival time at the surface after correction for the atomic photoemission delay of the adatom[10,11]. The light pulse simultaneously propagates into the crystal and photoexcites electrons from both localized core orbitals and delocalized conduction bands of W(110). Thus, Bloch wave packets in high-lying conduction bands evolve, and some travel towards the surface and exit the crystal. Using a defined near-infrared (NIR) electric waveform (temporal full-width at half-maximum $\tau_{\mathrm{FWHM}} \approx 4$ fs, carrier wavelength $\lambda_{\mathrm{carrier}} = 780$ nm), we encode the instant of an electron's appearance in the ionization continuum as an observable momentum modulation ('streaking'[8].). The NIR light is reflected and refracted at the metal surface such that the electric field components causing streaking are suppressed within the crystal[3]. Therefore, electrons originating from the crystal interior are only momentum-modulated once they have left the solid, and their sojourn time in the crystal can be retraced. The ångström-scale proximity of the chronoscope atoms to the surface eliminates uncertainties in the synchronization of the two light pulses due to Gouy phase differences, propagation and modification of the streaking field by reflection off the surface[12]. The last resulted in uncertainties of several tens of attoseconds in previous timing measurements of the photoelectron creation process[13,14]. We then gauge the emission delay of our clock atoms to achieve a true absolute delay timing. This is accomplished in a gas-phase streaking experiment using a mixture of chronoscope species and helium, illustrated in Fig. 1b. For the latter, the absolute photoemission delay is well tested and exactly computed by theory[15–17]. The complete experimental timing sequence is depicted in Fig. 1c.

Owing to its spectral isolation from helium and tungsten surface photoelectrons, we employ core-level photoemission from the 4*d* inner-shell orbitals of iodine (I4*d*) as a time-zero marker (see Fig. 2a, b). Core-level emission delays are largely independent of the chemical environment, as has been shown to hold for crystals[5]. The large photoabsorption cross-section of the I4*d* channel enhanced by the so-called giant dipole resonance allows for sufficient signal strength at a wide range of iodine coverage. Hence, we can quantify and eliminate residual transport and screening effects of the iodine overlayer by systematic variation of the adatom density and extrapolation to zero coverage. To obtain the moment of photon arrival at the surface from the chronoscope photoemission, the absolute I4*d* emission timing was determined in gauge measurements conducted on a gaseous mixture of small iodine-containing molecules and helium. Further considerations on the choice of chronoscope species, the gauge measurements, the comparability of molecular and adsorbate photoemission and the delay extraction method are detailed in Methods. The experimental setup is described elsewhere[18,19].

Experimental results are summarized in Figs. 1c and 2c. In the gas-phase gauge measurements, we find a relative delay of $\Delta\tau_{\mathrm{I4}d-\mathrm{He1}s} = (31 \pm 3)$ as between the escape of I4*d* and helium ground state (He1*s*) electrons. The absolute photoemission delay of photoelectrons escaping the 1*s* orbital in helium at 105 eV photon energy is[11,15] $\tau_{\mathrm{He1}s} = -5.0$ as. This yields an absolute I4*d* delay of $\tau_{\mathrm{I4}d} = \Delta\tau_{\mathrm{I4}d-\mathrm{He1}s} + \tau_{\mathrm{He1}s} = (26 \pm 3)$ as. All reported uncertainties represent 95% confidence. The delayed emission of I4*d* compared to He1*s* is mainly caused by an increased Eisenbud–Wigner–Smith (EWS) delay[20–22] due to the giant dipole resonance[23] (see also Methods).

[1]Physik-Department, Technische Universität München, Garching, Germany. [2]Max-Planck-Institut für Quantenoptik, Garching, Germany. [3]Helmholtz-Zentrum Berlin für Materialien und Energie, Berlin, Germany. [4]Institute for Theoretical Physics, Vienna University of Technology, Vienna, Austria. [5]These authors contributed equally: M. Ossiander, J. Riemensberger. *e-mail: marcus.ossiander@mpq.mpg.de; reinhard.kienberger@tum.de

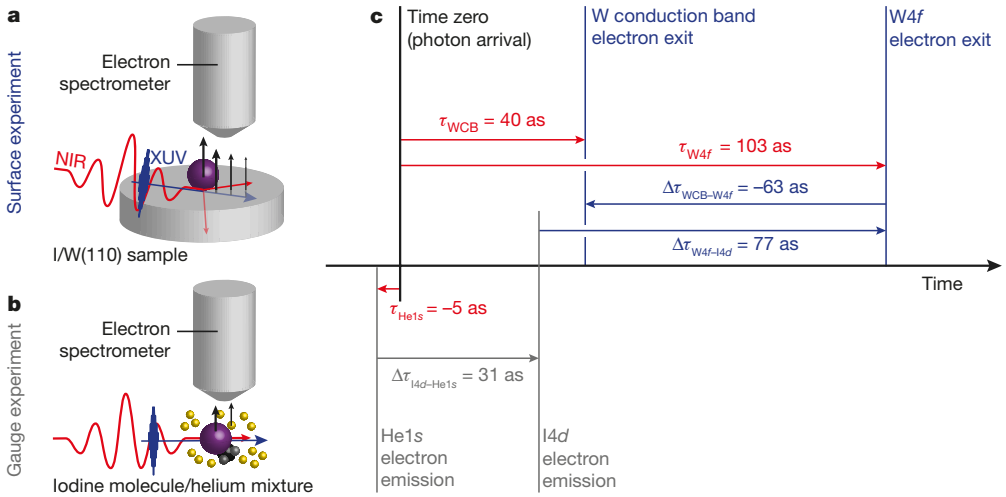

Fig. 1 | The atomic chronoscope method. a, Surface experiment. An XUV (blue) light pulse launches photoelectrons (black arrows) from a W(110) surface (grey) and from an iodine chronoscope (purple) on top. An NIR (red) laser pulse encodes the appearance time of photoelectrons above the crystal as a momentum shift, which is resolved using an electron spectrometer. **b**, Gas-phase gauge experiment. The delay between photon absorption by the chronoscope and photoelectron appearance is determined by comparing to helium (yellow). **c**, Full timing sequence. Absolute delays are depicted in red, surface-experiment delays in blue and gauge-measurement delays in grey.

With the absolute time reference at hand, we can precisely determine the absolute electron exit delay for tungsten 4*f* (W4*f*) core electrons escaping the W(110) surface. A linear fit to the data in Fig. 2c reveals a coverage-dependent exit delay of $\tau_{W4f}(\theta) = \Delta\tau_{W4f-I4d}(\theta) + \tau_{I4d} = (77 \pm 5)$ as $+ \theta(8 \pm 7)$ as $+ \tau_{I4d}$ for W4*f* electrons as a function of the fractional iodine surface coverage θ in units of saturated monolayers (sat. ML). Importantly, the small influence of the iodine adlayer on the delay over the wide range of examined coverages allows assessment of the behaviour of pristine W(110) via extrapolation, which yields an absolute W4*f* exit delay $\tau_{W4f}^{clean} = (103 \pm 6)$ as for a bare surface.

By contrast, the average valence-electron timing of iodine-covered W(110) (denoted I/W(110)) features appreciable coverage dependence due to spectral overlap of weakly bound electrons from iodine and the tungsten conduction band. We thus performed additional measurements on a pristine W(110) surface, and found a W4*f* to tungsten conduction-band (WCB) delay $\tau_{W4f-WCB}^{clean} = (63 \pm 6)$ as. Owing to the high XUV photon energy, we can observe emission from the full Brillouin zone without delay artefacts due to misalignment of the electron detection direction and streaking laser field polarization[24]. By referencing to the absolute W4*f* exit delay, we determine an absolute tungsten

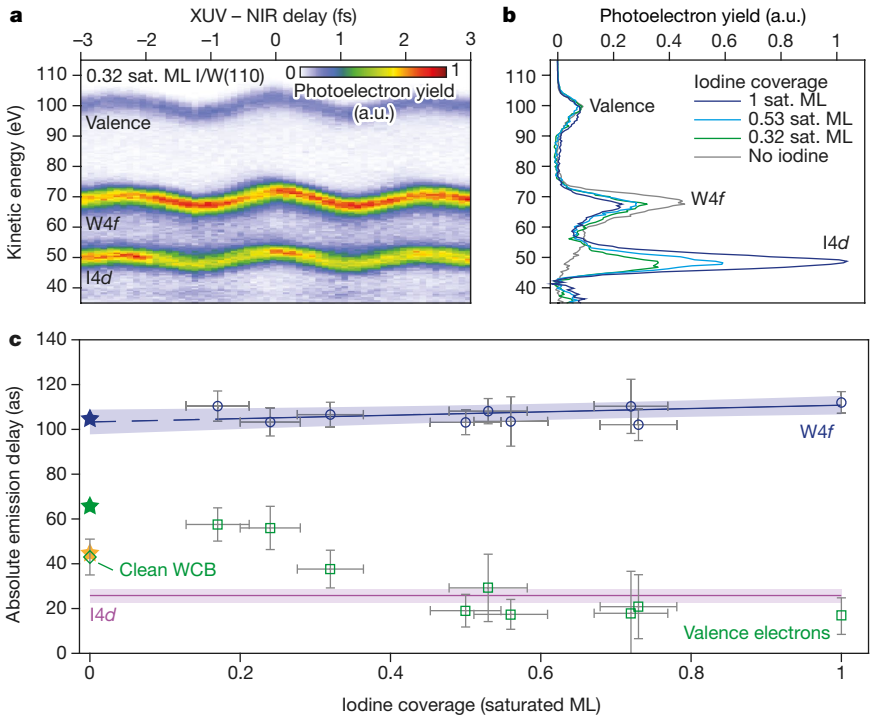

Fig. 2 | Absolute timing of W(110) photoemission at 105 eV photon energy. a, Representative I/W(110) streaking spectrogram. Delays are encoded as phase shifts of the kinetic-energy oscillations. **b**, XUV-only photoemission spectra for I/W(110) and pristine W(110). **c**, Iodine-coverage-dependent photoemission timing. Shown are W4*f* exit delay averages at coinciding iodine coverage (blue circles), the extrapolation to the pristine surface (blue line), I/W(110) valence-electron delays (green squares), the pristine W(110) conduction-band timing (green diamond), the I4*d* reference (purple) and transport simulation results (stars, W4*f* (blue), WCB with (yellow) and without (green) surface state influence). Errors represent 95% confidence intervals. Vertical error bars are calculated assuming a Student's *t*-distribution.

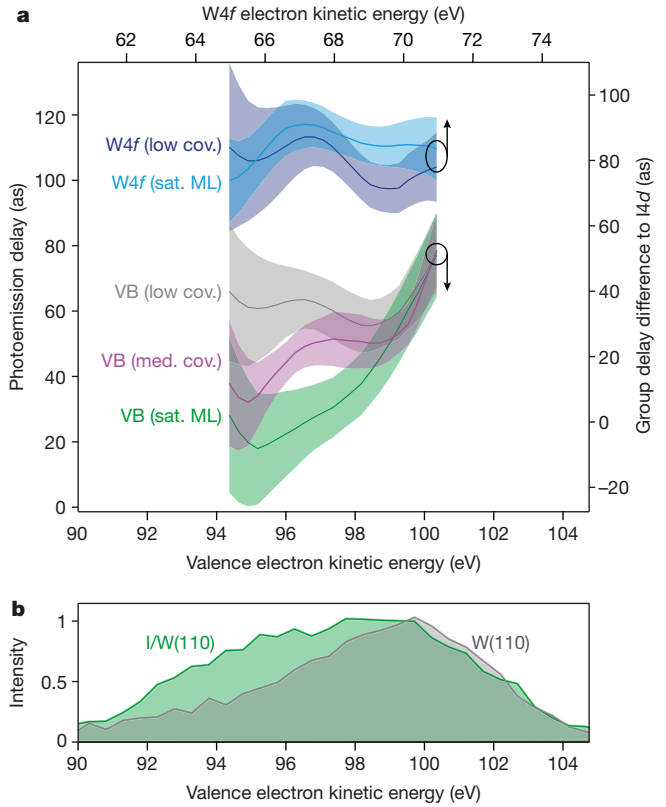

Fig. 3 | Timing of adsorbate photoemission. a, Energy-resolved emission delay of W4*f* core and I/W(110) valence-band (VB) photoelectrons for different iodine coverages. Core-level emission timing (blue lines) is unaffected by the iodine coverage (cov.) within the 95% confidence interval (shaded areas). The emission delay of valence states is substantially reduced, and its dispersion increases by adsorbing iodine (grey, purple and green lines). **b**, Photoelectron spectra of an iodine-saturated (green) and a clean (grey) W(110) surface. Iodine mainly contributes to the lower-kinetic-energy part of the valence-electron emission, visible in the spectra and in the energy-resolved photoemission delays.

conduction-band exit delay $\tau_{\mathrm{WCB}}^{\mathrm{clean}} = \tau_{\mathrm{W4}f}^{\mathrm{clean}} - \Delta\tau_{\mathrm{W4}f-\mathrm{WCB}}^{\mathrm{clean}} = (40 \pm 9)$ as. The small conduction-band photoemission delay for clean tungsten is surprising, as it is comparable to the EWS delay in gas-phase I4*d* photoemission.

A major advantage of absolute emission timing is that the duration of the creation process for each observed photoemission feature is individually recorded. Thus, all delay contributions, even those cancelling in relative measurements[25], are uncovered by the present absolute measurement, enhancing the importance of the extracted timing information for benchmarking theoretical models and allowing their direct interpretation. Tungsten inner-shell photoemission is reproduced quantitatively by transport simulations based on a three-step model (see Methods): the primary photoexcitation of a W4*f* electron contributes an EWS delay of about 10 as (see ref. [5] and its Supplementary Information). Subsequently, the electron propagates to the crystal surface and electron streaking starts at the jellium edge[3], located about 1.1 Å above the topmost tungsten layer. The average escape depth corresponds to the mean free path for inelastic scattering[26], approximately 4.1 Å. Adding the transport time for free-electron propagation to the EWS delay predicts a total exit delay of $\tau_{\mathrm{W4}f} = 85$ as, slightly less than measured in our experiment. Including inelastically scattered conduction-band electrons with an energy close to the W4*f* line yields 105 as, in almost perfect agreement with the measured data. This is markedly different from ref. [2], where a reduced group velocity for W4*f* electrons was proposed as a reason for the observed relative core-level to conduction-band delay for comparable emission angle integration at slightly lower photon energy.

Electron ejection from the conduction band proceeds substantially faster. Using the effective emission depth of photoionized conduction-band electrons[26], about 4.2 Å, predicts an exit delay of $\tau_{\mathrm{WCB}} = 66$ as for conduction-band electrons, considerably larger than measured. As the relevant band structure does not feature group velocities much larger than that of a free electron in the relevant energy region[27], we attribute the remaining discrepancy to a major contribution of surface states to the tungsten conduction-band emission. Surface states of W(110) have been studied theoretically[28] and experimentally[29]. Using density-functional-theory (DFT) calculations we identify surface states located in the surface bandgap of the clean substrate (see Methods). From their depth distribution, we determine an exit delay of $\tau_{\mathrm{SS}} \approx 11$ as. Including a surface state contribution with a spectral weight of 1/3 relative to the total conduction-band emission[29,30] in the transport simulation reduces the average conduction-band exit delay to $\tau_{\mathrm{CB}} \approx 45$ as and reproduces the experimental value for the pristine W(110) surface. In turn, quenching of surface states by adsorbates covering the surface can cause a larger exit delay and the non-monotonic behaviour of τ_{CB} at low coverages (Fig. 2c). These findings highlight that proper accounting for the initial creation, origin, transport and scattering of electrons is imperative for the proper description of the photoelectric effect.

To scrutinize the electronic dynamics of the adsorbate surface layer, we resolve the energy of the exit delays using a generalized-projection algorithm[15,31]. Results are presented in Fig. 3a. Spectrally averaged delays match those obtained from the original retrieval method. The valence photoelectron spectrum in Fig. 3b is dominated by emission from the tungsten conduction band in the high-kinetic-energy region and by adsorbate iodine valence states in the low-kinetic-energy flank, consistent with DFT calculations (see Methods). Whereas the tungsten conduction-band (high-energy region) delay is only marginally altered by the adsorption of chronoscope atoms, the adsorbate (low-energy flank) delay decreases with increasing iodine surface coverage. Comparing the photoemission delay for different adsorbate densities thus directly reflects the shift of the valence photoelectron origin from within the first crystal layers to the iodine above the surface. Accounting for residual contributions of the tungsten conduction band reveals an iodine valence (IV) photoemission delay of $\tau_{\mathrm{IV}} = (8 \pm 19)$ as. Atomic adsorbates therefore enable the creation of photoelectrons with negligible lag in time even from solid systems. The stability of the W4*f* timing proves that crystal core-state photoemission is robust against the addition of non-screening adsorbates. Hence, future studies can directly explore the time domain evolution of complex adsorbates by using the present surface core-electron results as a reference.

The atomic chronoscope is a viable tool with which one can determine the absolute timing sequence of the photoelectric effect in condensed matter systems. All terms contributing to its duration are captured, allowing the analysis of future measurements without ambiguity, even those performed on complex interfacial architectures. Clocking a photoelectron's creation is a direct gateway to its phase; hence our results complement and challenge our understanding of the electronic structure of solids, which has so far been shaped by spectral investigations. Surface-adsorbate systems could allow the creation of nanoscopic switches for molecular electronics, the improvement of the efficiency of chemical reactions using heterogeneous catalysis, or the inexpensive harvesting of solar energy. The initial dynamics that lead to photon absorption and subsequent chemical response are the key to systematic design of devices. The photoemission delay of adsorbates probes the local environment around the adsorption sites[32]. Delay measurements using the present technique and timing reference could thus serve as attosecond probes and help to unravel the non-equilibrium dynamics that initiate photochemistry.

Online content

Any methods, additional references, Nature Research reporting summaries, source data, statements of data availability and associated accession codes are available at https://doi.org/10.1038/s41586-018-0503-6.

Received: 12 April 2018; Accepted: 26 July 2018;
Published online 19 September 2018.

1. Damascelli, A. Probing the electronic structure of complex systems by ARPES. *Phys. Scr. T* **109**, 61–62 (2004).
2. Cavalieri, A. L. et al. Attosecond spectroscopy in condensed matter. *Nature* **449**, 1029–1032 (2007).
3. Neppl, S. et al. Direct observation of electron propagation and dielectric screening on the atomic length scale. *Nature* **517**, 342–346 (2015).
4. Seiffert, L. et al. Attosecond chronoscopy of electron scattering in dielectric nanoparticles. *Nat. Phys.* **13**, 766–770 (2017).
5. Siek, F. et al. Angular momentum–induced delays in solid-state photoemission enhanced by intra-atomic interactions. *Science* **357**, 1274–1277 (2017).
6. Chen, C. et al. Distinguishing attosecond electron–electron scattering and screening in transition metals. *Proc. Natl Acad. Sci. USA* **114**, E5300–E5307 (2017).
7. Tao, Z. et al. Direct time-domain observation of attosecond final-state lifetimes in photoemission from solids. *Science* **353**, 62–67 (2016).
8. Kienberger, R. et al. Atomic transient recorder. *Nature* **427**, 817–821 (2004).
9. Muller, H. G. Reconstruction of attosecond harmonic beating by interference of two-photon transitions. *Appl. Phys. B* **74**, s17–s21 (2002).
10. Schultze, M. et al. Delay in photoemission. *Science* **328**, 1658–1662 (2010).
11. Pazourek, R., Nagele, S. & Burgdörfer, J. Attosecond chronoscopy of photoemission. *Rev. Mod. Phys.* **87**, 765–802 (2015).
12. Lucchini, M. et al. Light-matter interaction at surfaces in the spatiotemporal limit of macroscopic models. *Phys. Rev. Lett.* **115**, 137401 (2015).
13. Locher, R. et al. Energy-dependent photoemission delays from noble metal surfaces by attosecond interferometry. *Optica* **2**, 405–410 (2015).
14. Kasmi, L. et al. Effective mass effect in attosecond electron transport. *Optica* **4**, 1492–1497 (2017).
15. Ossiander, M. et al. Attosecond correlation dynamics. *Nat. Phys.* **13**, 280–285 (2017).
16. Palacios, A., McCurdy, C. W. & Rescigno, T. N. Extracting amplitudes for single and double ionization from a time-dependent wave packet. *Phys. Rev. A* **76**, 043420 (2007).
17. Pazourek, R., Feist, J., Nagele, S. & Burgdörfer, J. Attosecond streaking of correlated two-electron transitions in helium. *Phys. Rev. Lett.* **108**, 163001 (2012).
18. Magerl, E. et al. A flexible apparatus for attosecond photoelectron spectroscopy of solids and surfaces. *Rev. Sci. Instrum.* **82**, 063104 (2011).
19. Cavalieri, A. L. et al. Intense 1.5-cycle near infrared laser waveforms and their use for the generation of ultra-broadband soft-X-ray harmonic continua. *New J. Phys.* **9**, 242 (2007).
20. Eisenbud, L. *The Formal Properties of Nuclear Collisions*. PhD thesis, Princeton Univ. (1948).
21. Wigner, E. P. Lower limit for the energy derivative of the scattering phase shift. *Phys. Rev.* **98**, 145–147 (1955).
22. Smith, F. T. Lifetime matrix in collision theory. *Phys. Rev.* **118**, 349–356 (1960).
23. Huppert, M., Jordan, I., Baykusheva, D., von Conta, A. & Wörner, H. J. Attosecond delays in molecular photoionization. *Phys. Rev. Lett.* **117**, 093001 (2016).
24. Heuser, S. et al. Angular dependence of photoemission time delay in helium. *Phys. Rev. A* **94**, 063409 (2016).
25. Neppl, S. et al. Attosecond time-resolved photoemission from core and valence states of magnesium. *Phys. Rev. Lett.* **109**, 087401 (2012).
26. Tanuma, S., Powell, C. J. & Penn, D. R. Calculations of electron inelastic mean free paths. II. Data for 27 elements over the 50–2000 eV range. *Surf. Interface Anal.* **17**, 911–926 (1991).
27. Krasovskii, E. E. Attosecond spectroscopy of solids: streaking phase shift due to lattice scattering. *Phys. Rev. B* **84**, 195106 (2011).
28. Mirhosseini, H., Flieger, M. & Henk, J. Dirac-cone-like surface state in W(110): dispersion, spin texture and photoemission from first principles. *New J. Phys.* **15**, 033019 (2013).
29. Pi, T.-W., Hong, L.-H. & Cheng, C.-P. Synchrotron-radiation photoemission study of Ba on W(110). *Phys. Rev. B* **58**, 4149–4155 (1998).
30. Riemensberger, J. *Time-Frequency-Resolved Absolute Time Delay of the Photoelectric Effect*. PhD Thesis, Technische Universität München (2018).
31. Yakovlev, V. S., Gagnon, J., Karpowicz, N. & Krausz, F. Attosecond streaking enables the measurement of quantum phase. *Phys. Rev. Lett.* **105**, 073001 (2010).
32. Kazansky, A. K. & Echenique, P. M. Theoretical study of the ionization of an alkali atom adsorbed on a metal surface by a laser-assisted subfemtosecond pulse. *Phys. Rev. B* **81**, 075440 (2010).

Acknowledgements We acknowledge discussions with M. Schultze, experimental support by A. Kim and A. Schiffrin and infrastructural support by F. Krausz. This work was supported by the Max Planck Society, the Deutsche Forschungsgemeinschaft Cluster of Excellence, Munich Centre for Advanced Photonics, a Consolidator Grant from the European Research Council (ERC-2014-CoG AEDMOS), LASERLAB-EUROPE (grant agreement number 654148, European Union's Horizon 2020 research and innovation programme), FWF Austria (SFB-041 ViCoM, SFB-049 NextLite) and COST Action CM1204 (XLIC). Calculations were performed using the Vienna Scientific Cluster (VSC).

Reviewer information *Nature* thanks M. Chini and T. Fennel for their contribution to the peer review of this work.

Author contributions M.O., J.R., S.N., M.M., M. Schäffer, A.D., M.S.W., R.H., M.W., M.G. and M. Schnitzenbaumer carried out the experiments. M.O. and J.R. analysed the experimental data. F.L., C.L. and J.B. performed the electron transport and DFT calculations. M.O. wrote the initial manuscript. J.V.B., P.F. and R.K. supervised the study. All authors discussed and reviewed the manuscript.

Competing interests The authors declare no competing interests.

Additional information
Extended data is available for this paper at https://doi.org/10.1038/s41586-018-0503-6.
Reprints and permissions information is available at http://www.nature.com/reprints.
Correspondence and requests for materials should be addressed to M.O. or R.K.
Publisher's note: Springer Nature remains neutral with regard to jurisdictional claims in published maps and institutional affiliations.

METHODS

Sample preparation and coverage calibration. Samples were prepared in situ in ~10^{-10} mbar ultrahigh vacuum. Commercially available polished W crystals with (110) oriented surfaces were cleaned via thermal annealing, argon ion sputtering, ten oxidation/desorption cycles in 10^{-6} mbar oxygen atmosphere and final annealing to 2,400 K for 20 s. Surface structure and cleanliness were scrutinized via low-energy electron diffraction and Al-Kα X-ray photoelectron spectroscopy. Gaseous molecular iodine was introduced into the preparation volume via sublimation of a solid piece of iodine that was thoroughly degassed using cryogenic distillation and several cycles of evaporation before the sample preparation. A saturated monolayer of iodine atoms[33] was adsorbed onto the crystal by dosing ~40 Langmuir of gaseous iodine. Iodine molecules dissociate upon adsorption in the first monolayer[34]. Subsequent growth of additional layers of iodine necessitates cryogenic cooling and is unstable to NIR irradiation due to the broadband visible light absorption of molecular iodine. Saturation was verified in the range between ~6 and ~30 Langmuir by photoelectron spectroscopy with XUV light. Submonolayer (non-saturated) coverages were created via subsequent thermal desorption of iodine[35] at temperatures up to 1,400 K and quantified via XUV photoelectron spectroscopy. Exemplary photoelectron spectra are presented in Extended Data Fig. 1a. The background of inelastically scattered electrons in the steady-state spectra in Extended Data Fig. 1a was subtracted using a Shirley background[36] in energy regions of primary electron emission and a constant background elsewhere. The background subtraction scheme is illustrated in the inset of Extended Data Fig. 1a.

Electron detection. Electron momentum spectra were recorded along the XUV polarization direction via time-of-flight spectrometry. An electrostatic lens assembly was employed during streaking spectroscopy to increase the energy-dependent electron acceptance angle during time-dependent measurements. The half-angle acceptance for electrons from the He1*s* and I4*d* electron energy region was ~10° in both measurements. The half-angle acceptance for W4*f* electrons was ~12°, and the half-angle acceptance for valence-band electrons was ~22°. Both streaking and RABITT measurements can suffer from delay distortions for large angles between the electron detection and the laser field polarization direction[24]. However, these only occur at substantially higher acceptance angles than employed in the present experiment. The energy-dependent lens transmission was corrected for before delay extraction.

Energy-averaged delay extraction. All delays reported were extracted using established algorithms[10]. A detailed discussion, validation and comparison to other delay extraction methods is found elsewhere[15]. Energy-averaged delays were retrieved by fitting the strong-field solution of the time-dependent Schrödinger equation[37] $P(E_f,\tau) \approx |\int_{-\infty}^{\infty} \mathcal{E}_{XUV}(t-\tau) d e^{i\phi_{Volkov}(\mathcal{E}_{NIR},E_f,t)} e^{-itE_i} e^{itE_f} dt|^2$ in the central-momentum approximation[31] to the experimental spectrograms. The streaked photoelectron spectrum $P(E_f,\tau)$ at final kinetic energy E_f and XUV–NIR delay τ is determined by the energy of the unstreaked continuum state E_i, the dipole matrix element d, the envelope of the attosecond pulse $\mathcal{E}_{XUV}$ and the NIR electric field $\mathcal{E}_{NIR}$ through the Volkov phase ϕ_{Volkov}. This technique prevents loss of information as in, for example, methods treating only the first moments in energy of the spectral distributions. The robustness of the method is increased by parametrizing all light and electron pulses as Gaussians with up to second-order phase. Inelastically scattered, non-streaking (that is, XUV−NIR-delay independent) background electrons are subtracted without any assumptions about their shape by taking the derivative along the XUV–NIR delay. The static shape of the photoemission features was fixed to synchrotron data[38,39] for stability. An individual electron wave packet group delay and chirp were fitted to each resolved spectral feature. Extended Data Fig. 2 shows a typical streaking spectrogram of the I/W(110) surface and its reconstruction.

Energy-resolved delay extraction. Energy-resolved photoemission delays were retrieved using a generalized-projections-type algorithm, similar to those employed in frequency-resolved optical gating, constructed following refs [31,40]. The algorithm is based on the same equations and approximations as above, but employs no assumptions about the phase or amplitude of the electron wave packets. To overcome the limitations of the central momentum approximation, several retrievals are run simultaneously at the central momenta of the individual photoemission lines. The retrievals are coupled in between steps by mixing the retrieved NIR waveforms, allowing accurate photoemission delays to be retrieved. Background caused by inelastically scattered electrons was subtracted before the retrieval using the Shirley scheme detailed in Methods section 'Sample preparation and coverage calibration'.

Iodomethane/iodoethane helium sample preparation. Gas-phase experiments were carried out on iodomethane or iodoethane mixed with helium. Iodomethane and iodoethane were bought from commercial suppliers (I8507, Sigma-Aldrich; I7780, Sigma-Aldrich). The stainless-steel cylinder containing these molecules was cooled using liquid nitrogen and then evacuated to remove residual air. Several mixing cycles were performed and discarded before each measurement to preserve purity. To maintain a stable backing pressure and helium/iodine-containing molecule ratio during the measurement, a large volume of gas mixture was prepared before the experiment. It was created by filling an evacuated reservoir up to the molecules' vapour pressure. This vapour was then diluted with helium until the desired ratio was achieved.

Overlap of molecular valence orbital electrons with He1*s* electrons. In our gas-phase reference measurement, the necessary spectral bandwidth of the XUV radiation causes spectral overlap of electrons emitted from the He1*s* and molecular orbitals. The same is true for the spectral overlap of shake-up photoemission from helium with electrons from I4*d* orbitals. Exemplary spectra of only iodoethane and a gas mixture are shown in Extended Data Fig. 3a. During the gas-phase experiments, the molecule/helium ratio was controlled such that both the helium shake-up states and the molecular orbitals yield only an ~5% contribution to the dominant I4*d* and He1*s* peaks, respectively. Retrieving the photoemission delay from simulated spectrograms containing overlapping photoemission features reveals that our retrieval method weights the photoemission delay of small spectral admixtures to a dominant feature quadratically with their intensity. Hence, the retrieval algorithm also extracts meaningful photoemission delays for the dominant part of a photoemission feature in the presence of small admixtures. Owing to their small photoemission intensity, molecular valence orbitals and helium shake-up satellites do not measurably influence the observed I4*d* and He1*s* delays, respectively. To verify this statement, we varied the ratio of helium to iodoethane in our measurements by more than a factor of four, leading to molecular orbital contributions to the helium peak of between 2% and 9%, see Extended Data Fig. 3b. We find no evidence of molecular orbital or helium shake-up influence on the measured photoemission delays, corroborating that the minor admixtures do not distort the results reported here.

Core-level photoemission from iodine on a surface and in a molecule. Not all photoemission delays from an atom in a molecule or on top of a surface are equivalent. Factors influencing delays in these different environments can be the hybridization and spectral overlap of orbitals, charge redistribution due to the chemical environment, scattering of electrons at other constituents of the molecule during their exit, alignment of the bond axis versus random bond orientation and modulation of the Coulomb–laser coupling due to screening by the metallic surface. We thus paid particular attention to the selection of our chronoscope species. This will be addressed in more detail below.

Hybridization and spectral overlap of atomic orbitals. To unambiguously extract the photoemission delay of a given atomic orbital, it should be spectrally separable from other orbitals in the spectrum. This fact prohibits the use of valence electrons as references in both stages of the experiment since their orbitals' shape and energy are not spectrally separable from surface valence electrons and, furthermore, are heavily influenced by the chemical environment. We therefore picked photoemission from the I4*d* core orbitals as an absolute time zero marker. Owing to its high binding energy, it is not involved in the bonding of the iodine to the surface or the molecule and is sufficiently spectrally separable from all surface and He1*s* photoemission features. Initial experiments were conducted using xenon adlayers, which also offer a usable 4*d* core level. However, all rare gases apart from He condense in islands upon physisorption, excluding the preparation of a homogeneous layer of clock atoms with variable coverage and density[41].

Orbital shape and charge localization. A change in the photoemission time delay could occur if the localization of electron charge around the core or the shape of the charge density were to change substantially. The I4*d* orbital shapes and hybridization with carbon or tungsten orbitals can be examined using quantum chemistry packages. We used GAMESS-US[42–44], a triple-zeta-basis set[45,46] and the CAM-B3LYP exchange–correlation functional[47] to calculate the I4*d* electron densities in different bound states. The overlap integral between corresponding I4*d* orbitals is >99% for iodine bound to CH_3 and W, stressing the immunity of the core orbital to external influences.

Electron scattering at the molecule and bond orientation. Further factors could influence the emission delay from the I4*d* orbitals: for example, the random molecular orientation with respect to the XUV radiation as compared to the aligned orientation on the surface, and the scattering of the continuum electron at the molecule during its exit. To estimate effects of both, we calculated the angle-dependent photoemission delay for I4*d* emission from iodomethane. For the calculations, we used GAMESS-US[42–44], a triple-zeta-basis set[45,46] and the local-density approximation[48] for the initial state, ePolyScat[49,50] for the photoionization and electron scattering calculations, and ePSproc[51] for the data analysis. ePolyScat has previously been applied for the extraction of molecular photoemission delays[23,51]. While scattering and angle dependence can have significant effects at low continuum electron energies, we find a maximum difference of less than 2 as between the orientation-averaged delay (the molecular case) and delay along the bond axis (the surface case) at 105 eV photon energy.

Giant dipole resonance properties. Molecular shape resonances arise in the absorption spectra of molecules and have been observed to contribute to the

photoemission delay[23]. These are fragile and susceptible to the chemical environment, that is, they disappear when the molecular structure is changed. By contrast, the spectral properties of atomic giant dipole resonances are largely independent of the chemical environment. The I4*d* giant dipole resonance position and width in atomic iodine and in iodomethane coincide[52,53]. Even the ionization state of atomic iodine has only minor influence, reinforcing the above statement[54]. Because the phase and amplitude properties of resonances are closely linked[55], a modification of the giant dipole resonance delay properties of iodine as adsorbate or in a molecule is unlikely.

Coulomb–laser coupling and image potential screening. The streaking time determined for the chronoscope atom iodine in the gas phase contains the contribution from the Coulomb–laser coupling (CLC)[11]. It is therefore important to inquire into the modifications due to adsorption at a metallic surface. Dynamical screening by conduction-band electrons will eventually shield the ionic core charge of the photoionized iodine, replacing the ionic potential, $-1/r$, entering CLC by an asymptotic Coulomb-like image potential, $-1/4z$. Here, r is the distance to the ion and z is the distance above the surface. This time-dependent dynamical screening potential[56] can be approximated in our exit delay simulation (see below) by a velocity (v) dependent potential experienced by the escaping electron, $V(z,v) = -\frac{1}{z}\exp\left(-\frac{w_s z}{v}\right) - \frac{1}{4z}\left[1-\exp\left(-\frac{w_s z}{v}\right)\right]$, with ω_s the surface plasmon frequency[57]. Since the dominant fraction of the CLC time shift is collected over the first few ångströms, the corrections due to dynamical screening at large distances are in the present case small. Uncertainties induced into the CLC timing by dynamical screening are found to be less than 3 as.

Gas-phase data. All individual gas-phase gauge measurements are summarized in Extended Data Fig. 3c. We find no change in the photoemission delay of I4*d* between iodoethane and iodomethane within the experimental uncertainty. This result suggests that the changes in intra-molecular photoelectron scattering and in the chemical environment do not affect the orientation-averaged photoemission delay from the I4*d* core orbitals. The increased photoemission time delay of the I4*d* orbitals compared to the He1*s* orbital is caused by the giant dipole resonance. It is created by a well-like effective photoelectron potential which can transiently trap the escaping electron[23,58].

I/W(110) data and delay dependence on coverage. All individual I/W(110) measurements are summarized in Extended Data Fig. 1b. Owing to the dielectric properties of the iodine layer, we do not expect a change in the streaking field near the surface and, hence, the W4*f* emission delay. Thus, we fit a linear function to the coverage-dependent photoemission delay results. The regression yields a W4*f* exit delay of $\Delta\tau_{W4f-I4d}(\theta) = (78 \pm 5)$ as $+\ \theta(8 \pm 7)$ as, which confirms near-negligible coverage dependence.

Pristine surface delay measurements. Measurements of the photoemission time delay of the W(110) surface were performed with the same XUV mirror as the iodine adsorbate and gas-phase measurements. Owing to the high reactivity of the tungsten surface, we investigated influences of surface contamination on the observed photoemission delay. Results are shown in Extended Data Fig. 1c. We find a weak increase (0.12 as min^{-1}) of the W4*f*—CB delay on the measurement time after preparation of a pristine tungsten surface. The relative photoemission time delay of the clean surface is recovered by linear extrapolation towards zero irradiation time of the W(110) crystal surface, which shows that W4*f* core-electron emission is delayed by $\tau^{\mathrm{clean}}_{W4f-\mathrm{WCB}} = (63 \pm 6)$ as with respect to emission from the conduction band.

DFT calculations. We employ DFT calculations using the VASP software package and the PBE exchange-correlation functional[59–62]. We use a cut-off energy of 230 eV in line with the PAW potentials for tungsten and iodine, and a minimum of $40 \times 40 \times 1$ k-points. After converging these parameters and the bulk lattice constant for a bulk supercell, we consider 8 layer W(110) slabs, with up to 72 W atoms (for the 3×3 supercell). Normal to the surface, the periodic images are separated by 45 Å of vacuum. The PAW potentials include 6 (7) active electrons for W (I), resulting in up to 453 active electrons for a 3×3 slab and three iodine atoms ($72 \times 6 + 3 \times 7 = 453$). All surface geometries are optimized by allowing the iodine atoms and the top three W layers to relax.

Semiclassical transport simulations. The timing of the electron emission is simulated by combining the atomic time delay given by the EWS time delay with the time delay due to the transport from the point of photoabsorption in the crystal to the arrival at the exit surface clocked by the NIR streaking field. Initial conditions for position and momenta for the transport simulation for the classical electron ensemble are derived from DFT calculations of the electron density and the density of states for the W(110) surface. Furthermore, the spectral width of the ionizing XUV pulse is included in the initial energy (and momentum) distribution of the electron departing from the site of photoabsorption. The subsequent transport of the electron distribution (or classical wave packet) through the medium takes into account interactions with ionic cores and electrons in terms of a stochastic sequence of scattering events[63], the properties of which are derived from doubly differential cross-sections for inelastic[26] and elastic scattering[64]. Following the trajectories until the photoelectron eventually escapes from the target surface, the escape time (transition through the jellium edge located half a lattice constant above the topmost layer) is recorded. Within this simulation, enhanced photoemission from surface states can be included by adding their contribution (as modelled by DFT) to the distribution of initial conditions. Streaking spectra are modelled by switching on the vector potential at escape time and adding it to the canonical momentum. Electron trajectories outside the acceptance angle of our detector are removed from the analysis. Different starting depths, different initial energies defined by the XUV spectrum, different transport lengths within the crystal due to the random scattering distribution and varying exit angles of the photoelectrons lead to a temporal broadening of the recorded electron wave packet adding to the XUV pulse duration. The simulation allows us to directly extract the microscopic average escape time from the solid. At the same time, it allows us to determine the time shift recorded by streaking spectra. We find agreement between the two within 5 as, thereby validating the interpretation of streaking time shift as photoemission timing information.

Tungsten surface state delay. To obtain an estimate of the delay expected for electrons emitted from surface states, we performed DFT calculations of a clean W(110) surface and investigated states within the surface bandgap. Extended Data Fig. 4a shows a 2D cut of the electronic density of the surface state. Streaking starts at the jellium edge, which is located 1.1 Å above the uppermost crystal layer. Relevant dimensions are indicated in Extended Data Fig. 4a. The inelastic mean free path, that is, the average escape depth for conduction-band photoelectrons in the presented experiment is approximately 4.2 Å, which would lead to an escape delay of $\tau_{\mathrm{WCB}} \approx 66$ as. The localization of the surface state close to the jellium edge results in an average crystal exit delay of only $\tau_{\mathrm{SS}} \approx 11$ as. Owing to the proximity to the surface, inelastic scattering only negligibly affects photoelectrons from the surface state.

Iodine and tungsten valence states. To scrutinize the origin of valence electrons in different energy regions, we calculated the energy-resolved density of states of an iodine covered W(110) surface via DFT. Results obtained for a 2×2 W + 2I slab (~86% saturated monolayer coverage) are presented in Extended Data Fig. 4b. The calculated DOS convoluted with the spectral width of the XUV source reproduces the experimental results. The density of states in the proximity of the tungsten surface atoms is mainly found in the first 3 eV below the Fermi edge E_{F}. Between 3 eV and 4 eV below the Fermi edge, the density of states is dominated by contributions found near the iodine adsorbates. These findings corroborate that the spectral differences observed in the experiment allow separation of the valence photoelectron feature into iodine and tungsten dominated spectral regions.

Data availability

The data that support the findings of this study are available from the corresponding authors upon request.

33. Jones, R. G. Halogen adsorption on solid surfaces. *Prog. Surf. Sci.* **27**, 25–160 (1988).
34. Jones, R. G. & Dowben, P. A. Reply to comments on "A re-interpretation of the LEED structures formed by iodine on W(110)" by P. A. Dowben and R. G. Jones. *Surf. Sci.* **116**, L228–L231 (1982).
35. Dowben, P. A. & Jones, R. G. A re-interpretation of the LEED structures formed by iodine on W(110). *Surf. Sci.* **105**, 334–346 (1981).
36. Shirley, D. High-resolution X-ray photoemission spectrum of the valence bands of gold. *Phys. Rev. B* **5**, 4709–4714 (1972).
37. Quéré, F., Mairesse, Y. & Itatani, J. Temporal characterization of attosecond XUV fields. *J. Mod. Opt.* **52**, 339–360 (2005).
38. Cutler, J. N., Bancroft, G. M., Sutherland, D. G. & Tan, K. H. Chemical dependence of core-level linewidths and ligand-field splittings: high-resolution core-level photoelectron spectra of I4*d* levels. *Phys. Rev. Lett.* **67**, 1531–1534 (1991).
39. Neppl, S. *Attosecond Time-Resolved Photoemission from Surfaces and Interfaces* (Technische Universität München, München, 2012).
40. Gagnon, J., Goulielmakis, E. & Yakovlev, V. S. The accurate FROG characterization of attosecond pulses from streaking measurements. *Appl. Phys. B* **92**, 25–32 (2008).
41. Dunin von Przychowski, M., Wiechert, H., Marx, G. K. L. & Schönhense, G. Real-space observation of xenon adsorption and desorption kinetics on graphite (0001) by photoemission electron microscopy. *Surf. Sci.* **541**, 46–58 (2003).
42. Schmidt, M. W. et al. General atomic and molecular electronic structure system. *J. Comput. Chem.* **14**, 1347–1363 (1993).
43. Schuchardt, K. L. et al. Basis Set Exchange: a community database for computational sciences. *J. Chem. Inf. Model.* **47**, 1045–1052 (2007).
44. Feller, D. The role of databases in support of computational chemistry calculations. *J. Comput. Chem.* **17**, 1571–1586 (1996).
45. Barbieri, P. L., Fantin, P. A. & Jorge, F. E. Gaussian basis sets of triple and quadruple zeta valence quality for correlated wave functions. *Mol. Phys.* **104**, 2945–2954 (2006).

46. Campos, C. T. & Jorge, F. E. Triple zeta quality basis sets for atoms Rb through Xe: application in CCSD(T) atomic and molecular property calculations. *Mol. Phys.* **111**, 167–173 (2013).
47. Yanai, T., Tew, D. P. & Handy, N. C. A new hybrid exchange correlation functional using the Coulomb-attenuating method (CAM-B3LYP). *Chem. Phys. Lett.* **393**, 51–57 (2004).
48. Perdew, J. P. & Zunger, A. Self-interaction correction to density-functional approximations for many-electron systems. *Phys. Rev. B* **23**, 5048–5079 (1981).
49. Natalense, A. P. P. & Lucchese, R. R. Cross section and asymmetry parameter calculation for sulfur 1s photoionization of SF_6. *J. Chem. Phys.* **111**, 5344–5348 (1999).
50. Gianturco, F. A., Lucchese, R. R. & Sanna, N. Calculation of low energy elastic cross sections for electron-CF_4 scattering. *J. Chem. Phys.* **100**, 6464–6471 (1994).
51. Hockett, P., Frumker, E., Villeneuve, D. M. & Corkum, P. B. Time delay in molecular photoionization. *J. Phys. B* **49**, 095602 (2016).
52. Nahon, L., Svensson, A. & Morin, P. Experimental study of the 4d ionization continuum in atomic iodine by photoelectron and photoion spectroscopy. *Phys. Rev. A* **43**, 2328–2337 (1991).
53. Olney, T. N., Cooper, G. & Brion, C. Quantitative studies of the photoabsorption (4.5–488 eV) and photoionization (9–59.5 eV) of methyl iodide using dipole electron impact techniques. *Chem. Phys.* **232**, 211–237 (1998).
54. Amusia, M. Y., Cherepkov, N. A., Chernysheva, L. V. & Manson, S. T. Photoionization of atomic iodine and its ions. *Phys. Rev. A* **61**, 020701 (2000).
55. Fano, U. Effects of configuration interaction on intensities and phase shifts. *Phys. Rev.* **124**, 1866–1878 (1961).
56. Burgdörfer, J. Dynamical image charge effects on convoy electron emission from solid surfaces. *Nucl. Instrum. Methods B* **24–25**, 139–142 (1987).
57. Weaver, J. H., Olson, C. G. & Lynch, D. W. Optical properties of crystalline tungsten. *Phys. Rev. B* **12**, 1293–1297 (1975).
58. Connerade, J. P. in *Giant Resonances in Atoms, Molecules, and Solids* (eds Connerade, J. P., Esteva, J. M. & Karnatak, R. C.) 3–23 (NATO Sci. Ser. B, Vol. 151, Springer Science+Business Media, New York, 1987).
59. Kresse, G. & Furthmüller, J. Efficient iterative schemes for ab initio total-energy calculations using a plane-wave basis set. *Phys. Rev. B* **54**, 11169–11186 (1996).
60. Kresse, G. & Joubert, D. From ultrasoft pseudopotentials to the projector augmented-wave method. *Phys. Rev. B* **59**, 1758–1775 (1999).
61. Kresse, G. & Hafner, J. Ab initio molecular dynamics for liquid metals. *Phys. Rev. B* **47**, 558–561 (1993).
62. Kresse, G. & Hafner, J. Ab initio molecular-dynamics simulation of the liquid-metal–amorphous-semiconductor transition in germanium. *Phys. Rev. B* **49**, 14251–14269 (1994).
63. Lemell, C., Solleder, B., Tőkési, K. & Burgdörfer, J. Simulation of attosecond streaking of electrons emitted from a tungsten surface. *Phys. Rev. A* **79**, 062901 (2009).
64. Salvat, F., Jablonski, A. & Powell, C. J. ELSEPA — Dirac partial-wave calculation of elastic scattering of electrons and positrons by atoms, positive ions and molecules. *Comput. Phys. Commun.* **165**, 157–190 (2005).

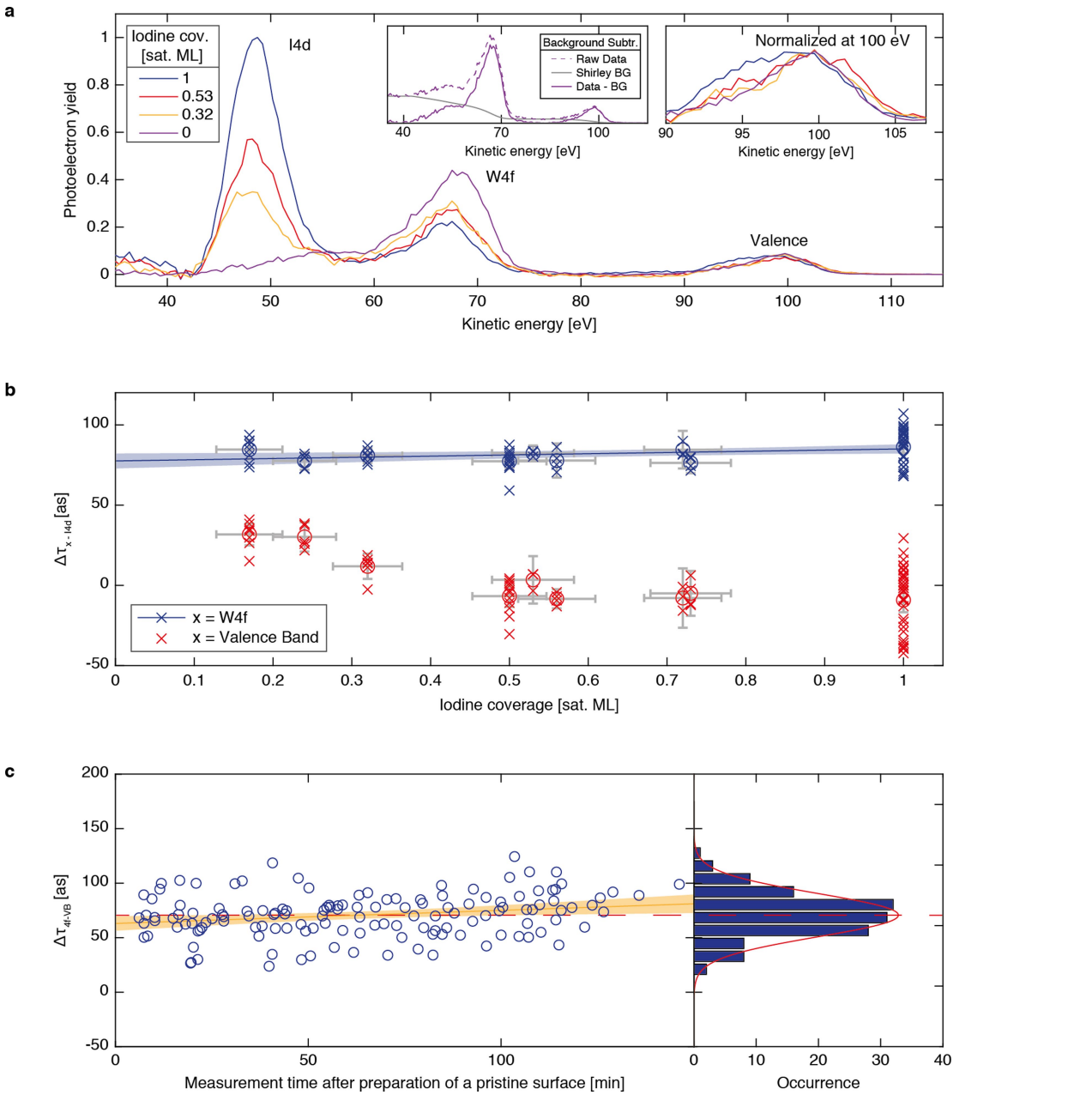

Extended Data Fig. 1 | I/W(110) and W(110) measurements. a, Main panel, XUV I/W(110) photoelectron spectra taken at 105 eV central photon energy for different adsorbate surface coverages (key in top left inset). Three effects are observable with decreasing iodine surface coverage: a decrease of the I4*d* peak intensity, an increase of the W4*f* peak intensity due to reduced inelastic scattering, and a shape change of the valence-electron peak towards a clean tungsten spectrum. The iodine surface density was calibrated by taking a full monolayer I/W(110) photoelectron spectrum as a reference before thermal desorption and comparing the I4*d* photoelectron flux before and after the thermal desorption of iodine. Because the iodine surface coverage saturates, this allows for a reliable coverage calibration. Top centre inset, illustration of the employed Shirley background (BG) subtraction scheme; top right inset, the magnified valence photoelectron spectrum. **b**, Relative photoemission delays for I/W(110). Both W4*f* to I4*d* (blue) and valence to I4*d* (red) delays are shown. All individual measurements are depicted by crosses, averages for individual coverages are depicted by circles. Vertical error bars mark 95% confidence assuming a Student's *t*-distribution and horizontal error bars mark maximum errors. The blue line represents a linear regression to the W4*f* to I4*d* delay (blue line), the shaded area represents the 95% confidence interval of this model. **c**, Attosecond streaking delay measurements on a pristine W(110) surface. The W4*f*−CB emission delay (blue circles and histogram) as a function of the time of measurement after the preparation of a pristine surface (yellow) reveals a small deviation of the centre (red, dashed line) of the normal distribution (red, solid line) fit to all measurements from the extrapolation to an instantaneous measurement due to surface contamination. The large number of measurements allows the extraction of the photoemission timing of the clean surface by extrapolation.

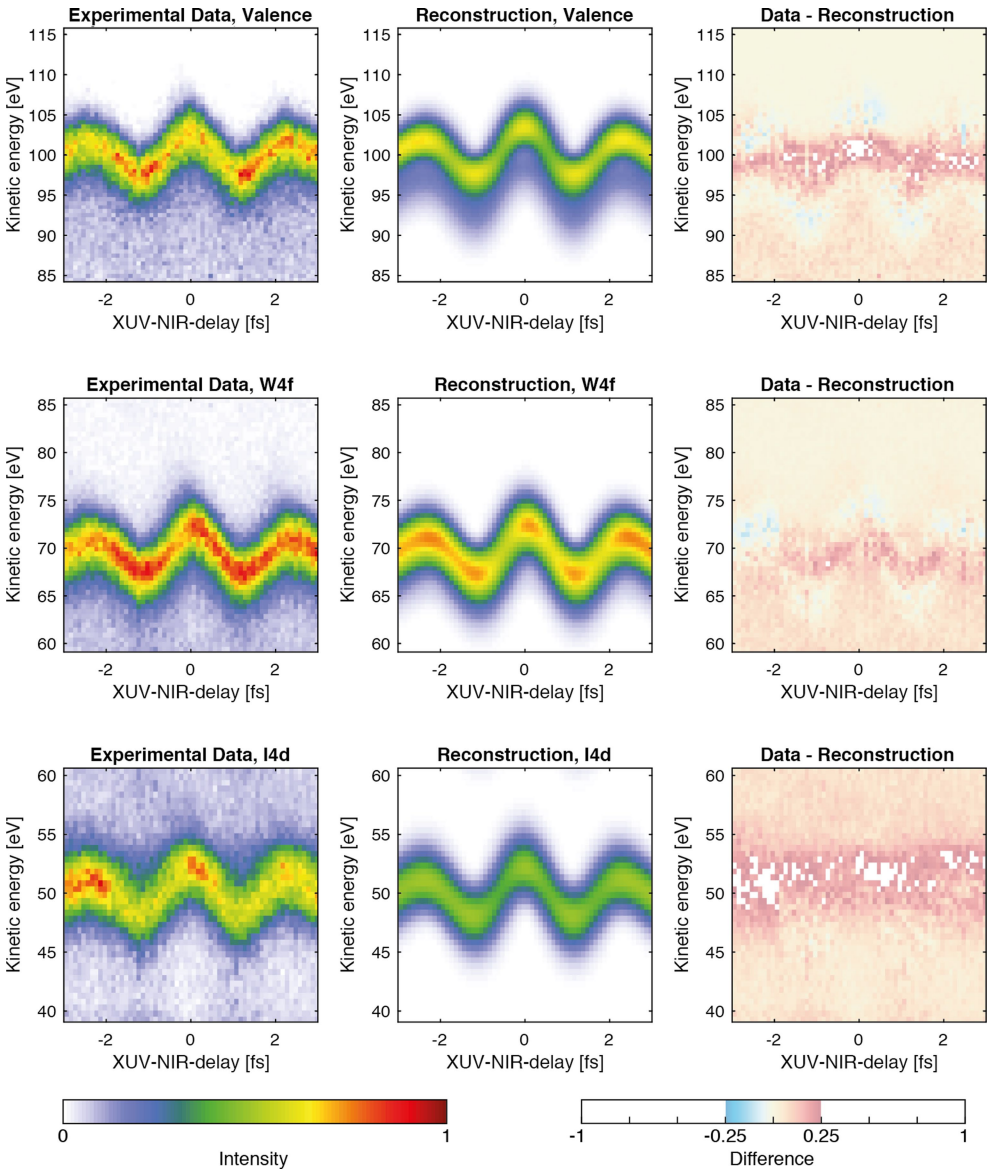

Extended Data Fig. 2 | Typical streaking spectrogram measured for I/W(110) at 32% of the saturated iodine surface coverage and its reconstruction. The first column shows the experimental data, the second column the results of the reconstruction algorithm and the third column their difference. The residual mainly consists of background independent of the XUV−NIR-delay, which is cancelled during the retrieval by differentiating along the delay axis. The three rows focus, from top to bottom, on the streaking of the valence, W4*f* and I4*d* photoemission peaks. The XUV−NIR-delay difference between consecutive spectra in the spectrogram is 200 as. The photoemission delay results extracted from this sample spectrogram are $\Delta\tau_{\mathrm{W4}f-\mathrm{I4}d} = 81$ as and $\Delta\tau_{\mathrm{Valence}-\mathrm{I4}d} = 14$ as.

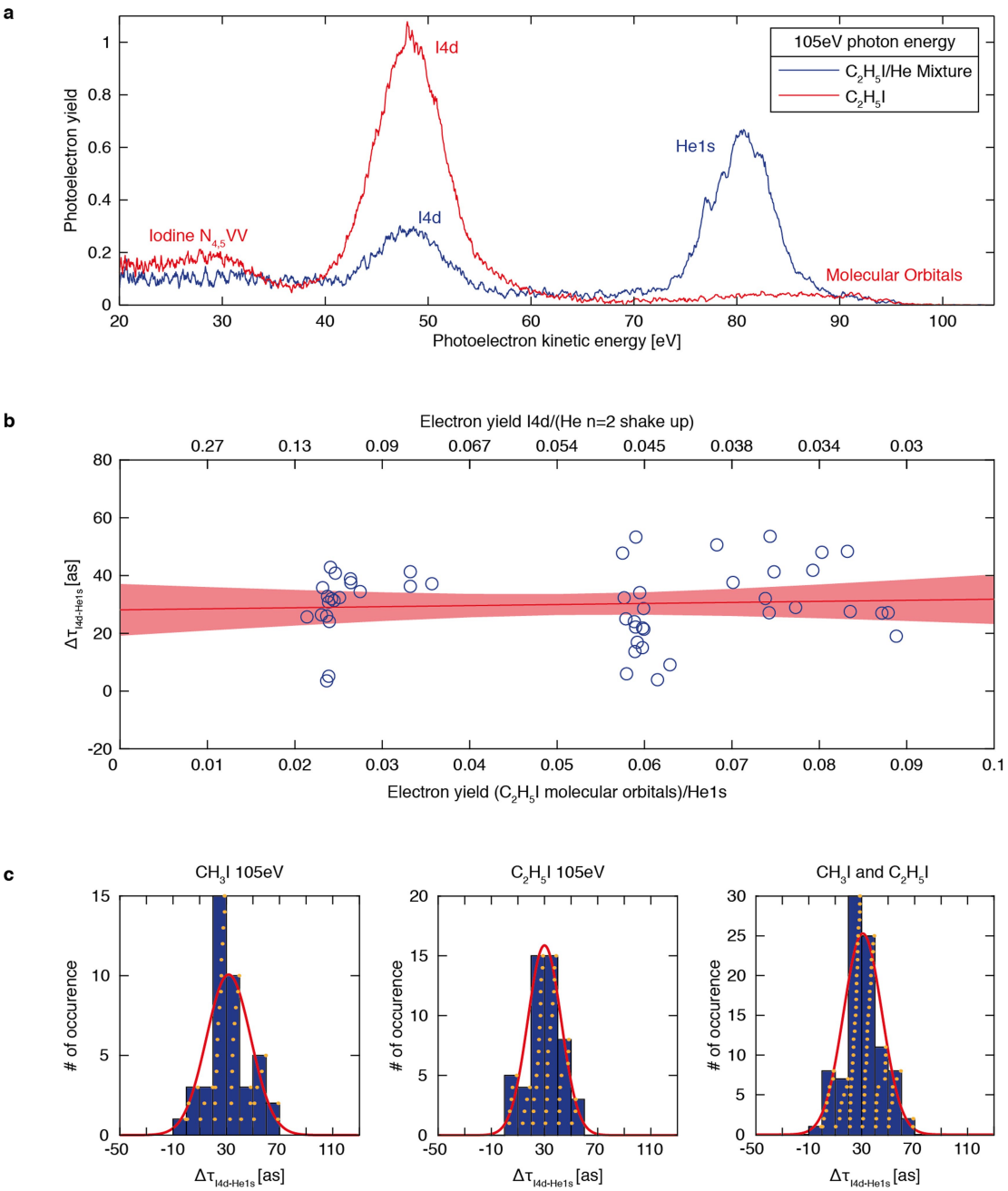

Extended Data Fig. 3 | Gas-phase iodine/helium measurements. **a**, Unstreaked XUV photoelectron spectra of iodoethane (red) and an iodoethane/helium mixture (blue) recorded at 105 eV central photon energy. Electrons emitted through the $N_{4,5}VV$ Auger process are spectrally separated from all timed photoelectron peaks. **b**, Relative I4*d*−He1*s* photoemission delay for different mixture compositions of iodoethane and helium. Shown are individual measurements (blue circles), linear regression (red line) and the 95% confidence interval of the regression (shaded area). **c**, Histograms (blue) of the individual relative photoemission delay measurements (yellow) between He1*s* and I4*d* electrons in iodomethane and iodoethane at 105 eV photon energy and normal-distribution fits to the data (red).

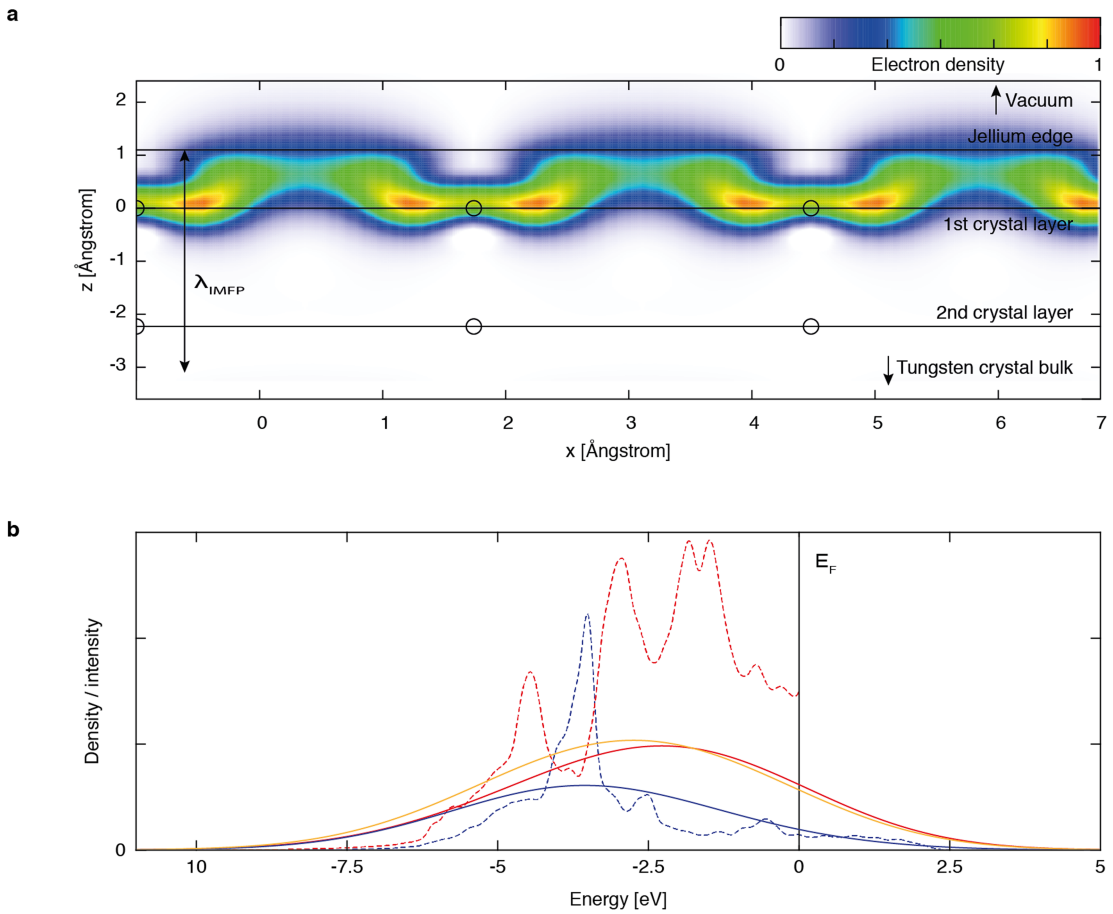

Extended Data Fig. 4 | Results of DFT calculations. a, DFT-derived electron density in the surface bandgap of a clean W(110) surface. A 2D cut through the $(1\bar{1}0)$ plane, perpendicular to the (110) surface, is shown. Tungsten atoms are indicated as black circles. Second-layer atoms are projected onto the plane of the cut. The inelastic mean free path λ_{IMFP} for conduction-band photoelectrons is marked as a guide to the eye. **b**, Energy-resolved density of states for an iodine-covered W(110) surface. The red dashed line represents the density of states in the proximity of the top-layer tungsten atoms and the blue dashed line represents the density of states near the iodine adsorbates. The full lines are folded with the spectrum of the experimental XUV pulse. The yellow line represents the full density of states of the iodine covered tungsten surface folded with the experimental XUV spectrum. See Methods for details of 'jellium edge' and E_F.